APPLIED SCIENCES AND ENGINEERING

Geometrically reconfigurable 3D mesostructures and electromagnetic devices through a rational bottom-up design strategy

Ke Bai[1], Xu Cheng[1], Zhaoguo Xue[1], Honglie Song[1], Lei Sang[2], Fan Zhang[1], Fei Liu[1], Xiang Luo[2], Wen Huang[2], Yonggang Huang[3], Yihui Zhang[1]*

Microelectronic devices with reconfigurable three-dimensional (3D) microarchitecture that can be repetitively switched among different geometrical and/or working states have promising applications in widespread areas. Traditional approaches usually rely on stimulated deformations of active materials under external electric/magnetic fields, which could potentially introduce parasitic side effects and lower device performances. Development of a rational strategy that allows access to high-performance 3D microdevices with multiple stable geometric configurations remains challenging. We introduce a mechanically guided scheme to build geometrically reconfigurable 3D mesostructures through a bottom-up design strategy based on a class of elementary reconfigurable structures with the simplest ribbon geometries. Quantitative mechanics modeling of the structural reconfigurability allows for the development of phase diagrams and design maps. Demonstrations of ~30 reconfigurable mesostructures with diverse geometric topologies and characteristic dimensions illustrate the versatile applicability. The multimode nature enables customized distinct beamforming and discrete beam scanning using a single antenna capable of on-demand reconfiguration.

INTRODUCTION

Reconfigurable microelectronic devices that can be reversibly switched between different geometrical and/or working states to realize distinct target functions have important applications in a broad range of areas, from wireless communication devices (*1*–*4*), energy absorption devices (*5*), optical devices (*6*–*8*), biomedical devices (*9*, *10*), to microelectromechanical systems (MEMS) (*11*–*14*) and robotics (*15*–*18*). Miniaturized switch components, such as radiofrequency MEMS switches (*19*–*22*), PIN diodes (*23*–*25*), and varactors (*26*–*28*), were widely exploited in the design of electrical circuits as a means to achieve the reconfiguration of device functionality. This strategy has enabled the development of reconfigurable devices with high switching speeds and small sizes, but these devices suffer from specific electrical issues, including the nonlinearity effects of switches, the noises, the power losses, as well as the complexity and other negative effects of the bias circuitry. Although the resulting devices can be reconfigured among a few different states, they can achieve the state switch only in a discrete manner and are usually unable to tune the device performance continuously in a broad range.

Strategies relying on the use of smart/active materials [e.g., shape memory polymers/alloys (*29*–*33*), phase transition materials (*34*), light sensitive materials (*35*–*37*), piezoelectric materials (*38*, *39*), magnetically responsive materials (*40*, *41*), dielectric elastomers (*42*, *43*), hydrogels (*44*–*46*), liquid crystal elastomers (*47*, *48*), and liquid metals (*49*, *50*)] provide another viable route to reconfigurable devices. When exposed to different external stimuli, such as electric/magnetic field, heat, and light, these materials undergo active deformations, which can be used to achieve reversible geometrical changes of patterned structures. The devices formed in this manner are thereby capable of adjusting the functionalities and/or performances that are sensitive to the geometric configurations. These mechanically guided reconfiguration strategies could avoid the negative effects induced by the use of switches and bias circuits and offer additional advantages in the continuous, wideband tunability of device performance. The requirement of specific operation environments (e.g., electric/magnetic fields) could potentially affect the performance of the functional devices, posing limitations in practical applications.

Here, we present a mechanically guided scheme and bottom-up design strategy to enable the construction of geometrically reconfigurable three-dimensional (3D) mesostructures on an elastomer substrate by using simple straight/curvy ribbon components as building blocks. This approach exploits the compressive forces induced by the release of biaxially prestrained substrate to drive the 3D transformation of patterned 2D precursors through a controlled, lateral buckling process (*51*–*54*). A previous work demonstrated that the use of simultaneous release and sequential release along a certain pair of orthotropic directions can provide possible access to distinct 3D configurations (*55*), thereby offering a route to achieve reconfigurable 3D mesostructures. However, this previous work only took into account the sequential release along a couple of limited directions and, thereby, did not provide a full picture of the structural reconfigurability through this approach. Consequently, the previous reconfigurable 3D mesostructures mostly involve quite intricate 3D geometries, as evidenced by the incorporation of creases (with reduced thickness) at various locations, and the demonstrated devices can be switched between only two operation modes. In the present work, we discovered a class of very simple ribbon elements (with only a single branch and two ends) that can be reshaped between distinct 3D configurations by analyzing quantitatively their reconfigurabilities under sequential release along all possible

[1]AML, Department of Engineering Mechanics, Tsinghua University, Beijing 100084, P.R. China. [2]School of Microelectronics, Hefei University of Technology, Anhui 230009, P.R. China. [3]Departments of Civil and Environmental Engineering, Mechanical Engineering, and Materials Science and Engineering, Northwestern University, Evanston, IL 60208, USA.
*Corresponding author. Email: yihuizhang@tsinghua.edu.cn

directions. The resulting phase diagrams of stable 3D configurations serve as a basis of the proposed bottom-up strategy to design complex reconfigurable mesostructures in the form of a linear/circular array, in which the rotational angle of each ribbon element can be optimized to obtain a desired number (e.g., from 2 to 10) of stable configurations. Combined experimental and computational studies of ~30 diverse examples, including those that consist of very simple ribbon geometries but offer more than three distinct stable configurations, illustrate the powerful capability of the proposed design strategy. Demonstrations of functionally reconfigurable 3D antennas for energy harvesting and communication suggest a broad range of application opportunities. In particular, the developed single antenna offers unique beamforming that can be switched among nine distinct modes and discrete beam scanning that can cover almost all in-plane directions, which is unachievable previously.

RESULTS

Conceptual illustration

Figure 1A illustrates the key concept of the scheme to achieve geometrically reconfigurable 3D mesostructure by extending the approach of buckling-guided assembly. This idea begins with a 2D precursor (left bottom frame of Fig. 1A) that can be patterned using techniques of laser cutting or photolithography (see fig. S1 for details), and an elastomer substrate with an equal biaxial prestrain (ε_{pre}). The 2D precursor consisting of a bilayer of aluminum (Al) (1 μm) and polyimide (PI) (25 μm) is bonded onto the surface (i.e., *xy* plane in the coordinate system in Fig. 1A) of prestrained elastomer selectively at two free ends. Through the use of a customized four-axis stretcher (see fig. S2 for details), the biaxial prestrain in the substrate can be released along four different sequential paths, which can be characterized by the loading angle (φ = 45°, 90°, 135°, or 180°, defined as the counterclockwise angle rotated from the positive direction of the *x* axis; see Fig. 1A) during the first step of prestrain release. Release of the remnant prestrain along an orthotropic direction (φ + 90° for $\varphi \leq 90°$ and φ − 90° for $\varphi > 90°$) in the second step ensures a complete release of the biaxial prestrain. Figure 1A shows that the sequential paths with φ = 45° and 135° lead to the formation of the same 3D configuration, referred to as mode I, the "fall" mode, which coincides with that which resulted from an end-to-end compression. The path with φ = 90° gives rise to a completely different 3D configuration (i.e., mode II, the "rise" mode), due to the shear buckling induced by the first step of the prestrain release. Owing to the ultrathin feature of the ribbon, as evidenced by the small aspect ratio (<0.01) of the thickness to the end-to-end distance, the maximum principal strains in the ribbon are well below the yield strains of the materials (0.3% for Al and 3% for PI), indicating the various buckling processes are all governed by elastic deformations (fig. S3). Consequently, the mesostructure can be reshaped reversibly between the modes I and II configurations through this sequential loading scheme. It is also noteworthy that the strain is uniformly distributed in a majority of the central region of the elastomer substrate (fig. S4A), which facilitates the design of parallel assembly for multiple reconfigurable 3D mesostructures, as shown subsequently in Fig. 1 (B and F). Excluding the above four sequential paths, an arbitrary sequential path with φ in the range of $(0,180°]\varphi \in (0,180^{o}]$ can be realized by rotation of the substrate with respect to the assembly platform (fig. S4B). Quantitative mechanics modeling based on finite element analysis (FEA) allows for the construction of the phase diagram that shows the stable 3D configurations for all possible release angles (φ). Excluding the range of $72° \leq \varphi \leq 117°$ that yields mode II, all of the other release angles give rise to mode I. This phase diagram suggests the rotational patterning of the above ribbon mesostructure (e.g., into a circular array) as a powerful bottom-up route to reconfigurable mesostructures with multiple stable 3D configurations. Figure 1B provides a demonstrative example with four different 3D configurations, where the 2D precursor consists of three pairs of ribbon mesostructures in Fig. 1A. Because of the central symmetry, the two ribbon components in each pair undergo the same deformations during the assembly. The pair 1 ribbon components have the same directionality (with respect to the coordinate system) as the mesostructure in Fig. 1A and, therefore, exhibit the rise mode only when $72° \leq \varphi \leq 117°$. Similarly, the pairs 2 and 3 ribbon components exhibit the rise mode only when $132° \leq \varphi \leq 177°$ and $12° \leq \varphi \leq 57°$, respectively. This can be clearly elucidated by the phase diagram in the bottom right panel of Fig. 1B, where the inner, middle, and outer layers correspond to the pairs 1 to 3 ribbon components, respectively. Such a phase diagram indicates that the entire mesostructure array exhibits four different stable 3D configurations. Note that all ribbon components in the array show the fall mode, when $0° \leq \varphi \leq 12°$, $57° \leq \varphi \leq 72°$, $117° \leq \varphi \leq 132°$, or $177° \leq \varphi \leq 180°$.

On the basis of the geometry in Fig. 1A, an energy-harvesting coil antenna whose operation mode could be adjusted by the release paths (φ) is designed (Fig. 1C), with the orange, blue, and red colors denoting the metallic layer (Cu, 6-μm thickness), supporting layer (PI, 25-μm thickness), and bonding sites. The chip capacitor (430 pF, for adjusting the resonant frequency of the secondary coil to 13.56 MHz) and the chip light-emitting diode (LED; red light) are connected to the metallic layer by welding. A planar primary coil attached onto the bottom surface of the substrate serves for energy transmission. Between the two different operation modes (Fig. 1D), the induced voltages in the coil antenna have a huge difference, due to the distinct distance and angle of the secondary coil with respect to the primary coil. Consequently, the on/off state of the LED can be switched reversibly by using different sequential release paths, i.e., "off" for $60° \leq \varphi \leq 120°$ and "on" otherwise. The quantitative calculations of induced voltages at the different modes that are normalized by the voltage value in the initial planar state of the coil antenna (Fig. 1E and fig. S5) show a contrast by more than an order of magnitude. Figure 1F and fig. S6B present a 3 × 3 array of energy-harvesting coil antennas inspired by the bottom-up design strategy, where the direction of each coil antenna has been optimized according to the phase diagram in fig. S6A. The resulting design in Fig. 1 (G and H) allows the array to offer 10 distinct operation modes. Three typical modes display the letters "T," "H," and "U" (Fig. 1, I and J), and the other operation modes (such as the letters "1," "11," and "□") appear in fig. S6C. The dynamic processes are shown in movie S1. The strain analysis and cyclic fatigue test of the coil antenna show that the device reconfiguration is reversible (figs. S7 to S9). The excellent compatibility of this approach with well-developed planar fabrication techniques suggests many application opportunities.

Phase diagrams and design maps for a class of simple reconfigurable 3D ribbon-shaped elements

Unveiling the reconfigurability of elementary mesostructures with very simple geometries is essential to the above bottom-up design

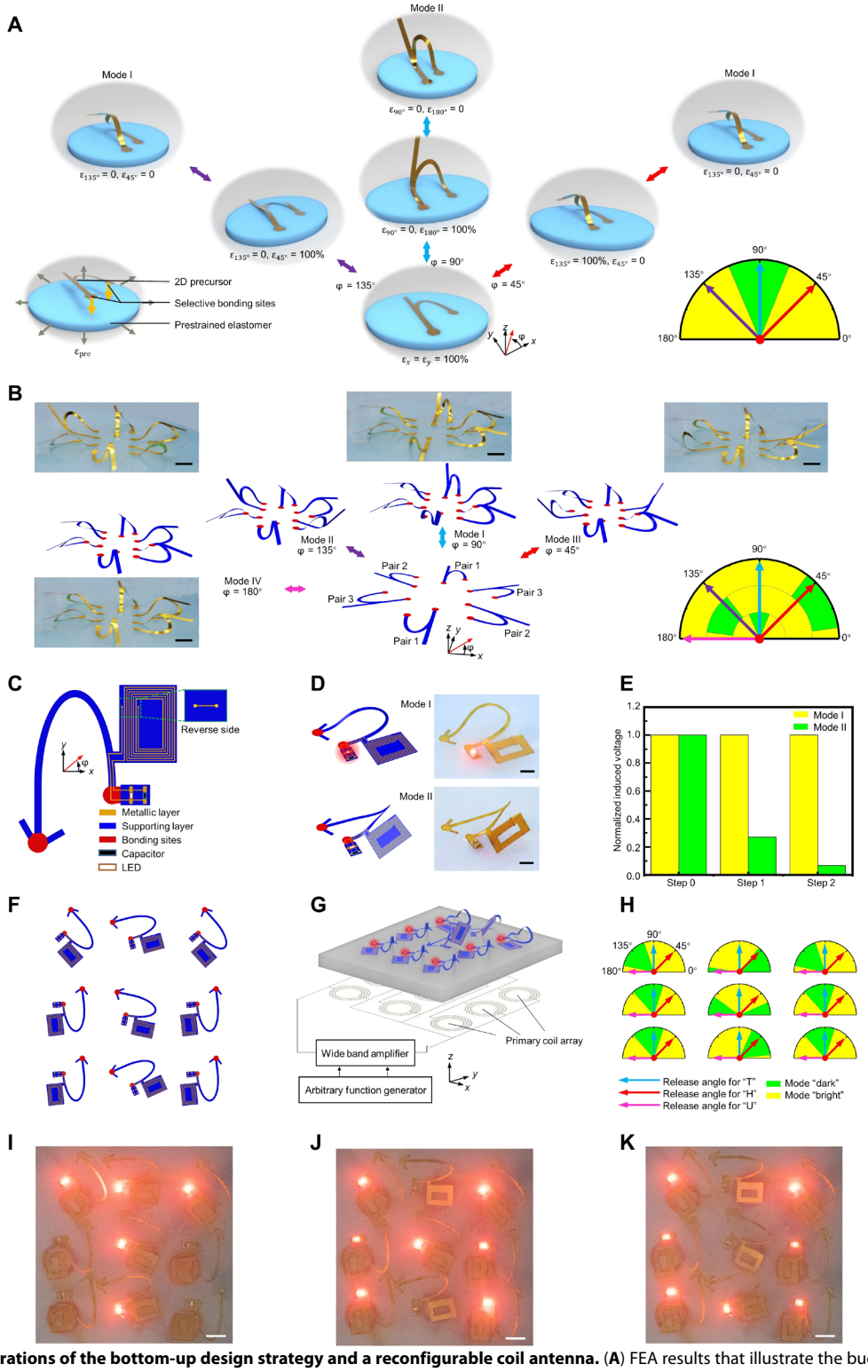

Fig. 1. Conceptual illustrations of the bottom-up design strategy and a reconfigurable coil antenna. (**A**) FEA results that illustrate the buckling-guided process to achieve a geometrically reconfigurable 3D mesostructure. The bottom right panel presents a phase diagram of stable 3D configurations at different release angles (φ), with yellow and green denoting modes I and II, respectively. (**B**) FEA results and optical images that show a 2D precursor consisting of three pairs of elementary mesostructures in (A), which can be transformed into four distinct 3D configurations. The bottom right panel presents a phase diagram consisting of three layers, with each layer showing the mode distribution of a pair of elementary mesostructures. (**C**) Schematic illustration of the 2D precursor design of a reconfigurable coil antenna. (**D**) FEA results and optical images of the 3D coil antenna at two different operation modes. (**E**) Normalized induced voltage of the coil antenna for φ = 90° and 180°. (**F** and **G**) Schematic illustration of a reconfigurable energy-harvesting device with a 3 × 3 array of basic elements. (**H**) Phase diagram for each element in the array. (**I** to **K**) Three different operation modes of the antenna array, as marked in (H). Scale bars, 2 mm. Photo Credit: K.B., Tsinghua University.

strategy. This section focuses on the 2D precursors consisting of a single curvy ribbon with only two ends, which can be regarded as the simplest type of ribbon geometries. Specifically, the fundamental categories of ribbon geometries, with shapes of an arc/elliptic segment, its combination with a straight segment, or a combination of two arcs with different arc angle/radii, are considered.

Figure 2 (A to D) presents the analysis of an arc-shaped 2D precursor with a constant curvature radius (R), where θ, t, and w denote the central angle, the thickness, and the width, respectively. Assuming the right end (bonding B) of the ribbon to be fixed during the sequential release of the substrate, the trajectory of the left end (bonding A) can be characterized by its two in-plane displacement components (u_x and u_y). Figure 2B shows such a trajectory for four typical sequential loading paths (φ = 45°, 72°, 135°, and 180°). Here, $\overline{u}_x$ and $\overline{u}_y$ are normalized by the displacement $[2\varepsilon_{pre}R\sin\theta/(1+\varepsilon_{pre})]$ of bonding A at the final release of the biaxial prestrain, i.e., $\overline{u}_x = u_x/[2\varepsilon_{pre}R\sin\theta/(1+\varepsilon_{pre})]$ and $\overline{u}_y = u_y/[2\varepsilon_{pre}R\sin\theta/(1+\varepsilon_{pre})]$. For each loading path, the trajectory consists of two perpendicular straight lines, with the intersection point corresponding to the end of the first step in the sequential loading. As the beginning and ending points are the same for all loading paths, the intersection points of different paths are located on the same circle (the dash circle in Fig. 2B), representing an envelope line of all possible loading paths. Considering the slender geometries (e.g., $t/w < 8, w/R < 8$), the Euler beam theory captures the spatial bending/twisting deformations of the curvy ribbon during the process of 3D transformation. Figure 2C and fig. S10 provide simulation results of FEA on the distributions of twisting curvatures and bending curvatures in a typical arc-shaped ribbon (θ = 1.7π), after the first and second steps of prestrain release for the four loading paths in Fig. 2B. For the path (φ = 72°) that yields mode II eventually, the distribution of twisting curvature after the first step of prestrain release only has a single minimum point (excluding the two ends), rather than multiple minimum points that emerge in the other cases (φ = 45°, 135°, and 180°; corresponding to mode I eventually). Associated deformation sequences of the elastomer substrate for these four release angles appear in fig. S11. The distributions of twisting curvature in ribbon precursors with four different central angles (θ = 0, 0.5π, π, and 1.5π) provide further evidence about this characteristic (Fig. 2D and fig. S12), i.e., single minimum point for mode II (eventually), in comparison to multiple ones for mode I.

Figure 2E and fig. S13 elucidate the physical mechanism of the geometrical reconfiguration through the sequential loading scheme. Here, a representative arc angle (θ = 1.7π) is taken for illustration, and four release angles (45°, 72°, 135°, and 180°) are considered. The formation of two distinct stable 3D configurations at different release paths can be attributed to the symmetry break induced by the supporting substrate. Specifically, without the mechanical interaction of supporting substrate, the final 3D shapes after the sequential releases with φ = 72° and 180° show a mirror symmetry, as evidenced by the curvature distribution (fig. S13). The assembled 3D shapes (mode I for φ = 180° and mode II for φ = 72°) with consideration of the substrate can be obtained by lifting the substrate from a location underneath the configurations at stage 2 (Fig. 2E), resulting in asymmetric deformations. All of the simple ribbon geometries studied in Fig. 2 follow this physical mechanism, with four additional examples provided in figs. S14 and S15.

Quantitative mechanics modeling based on FEA allows for the construction of a phase diagram (Fig. 2F) for the arc-shaped ribbon mesostructures in the space of geometric parameter (central angle θ) and loading parameter (release angle φ). For the central angle (θ) smaller than ~1.3π, the arc ribbon shows a unique stable mode for any release angles and, therefore, does not offer reconfigurability through the sequential loading scheme presented in this work. In the case of θ > 1.3π, the assembled mesostructure displays the mode II configuration with two peaks (middle right panel of Fig. 2F) for an intermediate range of release angle (around 90°), rather than the mode I configuration with a single peak (rightmost panel of Fig. 2F). The experimental results in Fig. 2F provide evidence about the validity of the phase diagram.

Figure 2G presents the design map for another fundamental category of simple 2D precursor consisting of a symmetric elliptic segment (semimajor axis a, semiminor axis b, and central angle θ), where the design space capable of 3D reconfiguration is identified. A design is regarded as "not reconfigurable" when it leads to a unique stable 3D configuration for any possible sequential release angles discussed above; otherwise, the design is reconfigurable through the sequential loading scheme. The results of assembly experiments carried out using three representative design parameters marked in Fig. 2G agree well with the predicted reconfigurability (Fig. 2H). The design map suggests that the range of central angle (θ) to render reconfigurability enlarges with the increase in the aspect ratio (a/b). Figure 2I and fig. S16 provide the validated design map for the ribbon 2D precursors consisting of an arc (central angle θ and radius R) and a straight segment (length l). In this case, a sufficiently large arc angle (θ) and a proper aspect ratio (l/R) are required to offer the reconfigurability. Figure 2J and fig. S17 provide the validated design map for the ribbon 2D precursors consisting of two arc segments with different central angles (θ_1 and θ_2) and radii (R_1 and R_2; $R_2 \geq R_1$), involving three dimensionless geometric parameters: θ_1, θ_2, and R_2/R_1.

For the fundamental categories of bistable ribbon designs in Fig. 2, a quantity K, defined as the product of two normalized bandwidths of release angle, i.e., $\varphi_I^{Bandwidth}/(\pi/2)$ and $\varphi_{II}^{Bandwidth}/(\pi/2)$, corresponding to modes I and II, i.e., $K = 4\varphi_I^{Bandwidth}\varphi_{II}^{Bandwidth}/\pi^2$, measures the degree of reconfigurability through the sequential loading scheme. Figure 2K presents a contour plot of this quantity (K) for a type of ribbon precursor consisting of a semiellipse segment and a straight segment. In the reconfigurable design space ($K > 0$), the degree of reconfigurability is enhanced at a larger aspect ratio (a/b). The results of experiments carried out using five representative design parameters marked in Fig. 2K are in good agreement with the predicted reconfigurability (Fig. 2L). For substrate prestrains of practical interests in the 3D assembly, e.g., > 10%, the phase diagrams remain unchanged at different levels of the prestrain (fig. S18), for all of the five representative designs marked in Fig. 2K.

Representative reconfigurable 3D mesostructures through the bottom-up design strategy

With the above simple ribbon geometries as building-block elements and their phase diagrams as a guideline, complex, multimodal, and reconfigurable 3D mesostructures can be built through a bottom-up design strategy.

Figure 3A and fig. S19 present a set of designs that involve mirror and duplication of the elementary ribbon mesostructures. For example, the first design exploits a mirror pattern of the ribbon element in Fig. 2K, i.e., a curvy ribbon combining a semiellipse segment and a straight segment ($a/b = 2$ and $l/b = 1$). The release

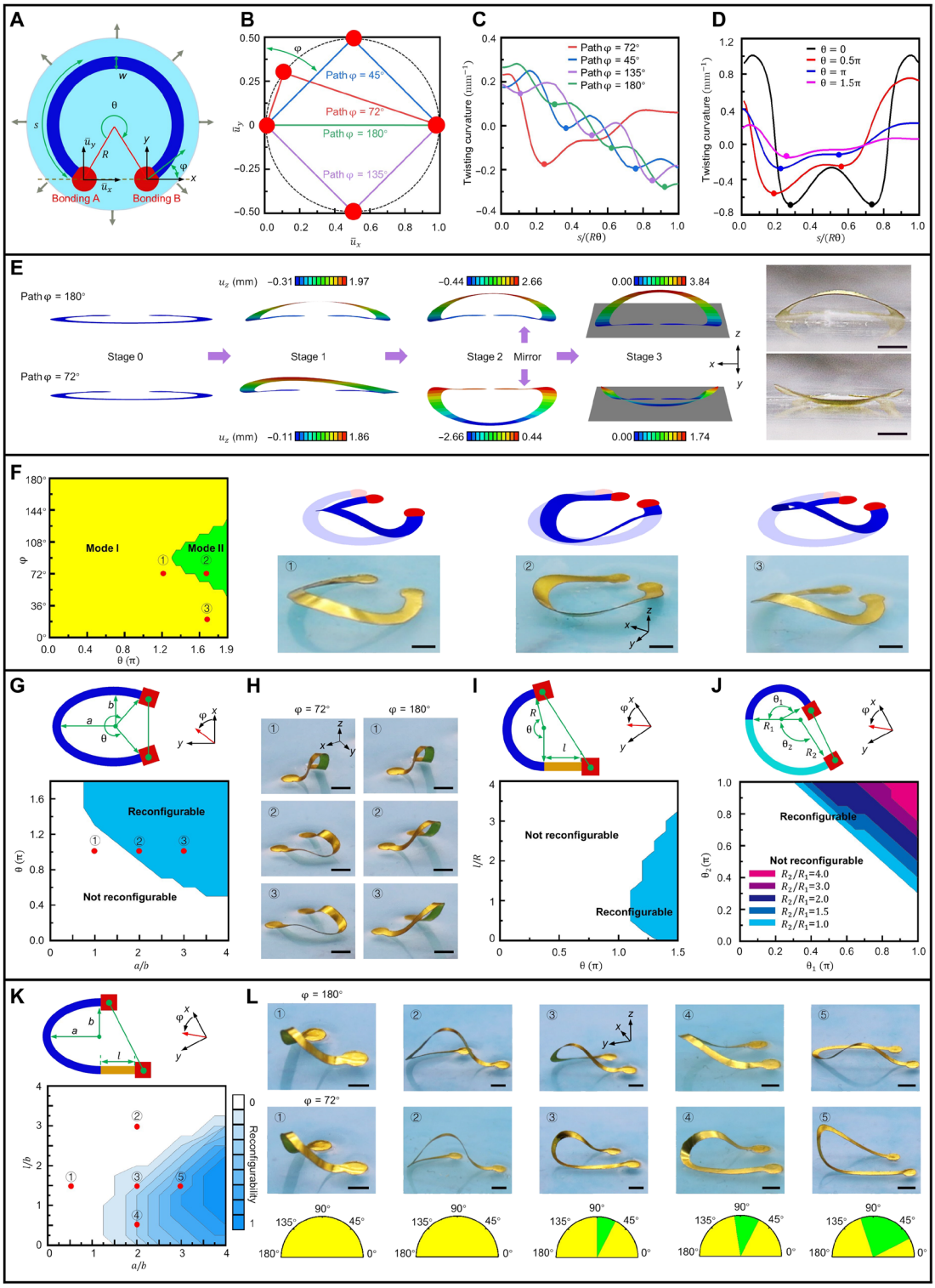

Fig. 2. Physical mechanisms and design maps of elementary, reconfigurable 3D mesostructures. (**A**) Schematic of an arc-shaped 2D ribbon precursor bonded onto a prestrained substrate. (**B**) Illustration of release paths for four typical release angles. (**C**) Distributions of twisting curvatures in the ribbon ($\theta = 1.7\pi$), after the first step of prestrain release. (**D**) Similar results for a fixed release angle ($\varphi = 72°$). (**E**) FEA results and optical images that illustrate the symmetry break induced by the appearance of the supporting substrate, leading to two distinct stable 3D configurations. (**F**) Phase diagram for the arc-shaped 2D precursor, along with optical images of assembled mesostructures in three representative conditions. (**G** and **H**) Design map for the 2D precursor consisting of a symmetric elliptic ribbon and optical images for three representative design points. (**I**) Design map for the 2D precursor consisting of an arc ribbon and a straight ribbon. (**J**) Similar results for the 2D precursor consisting of two arc ribbons with different central angles and radii. (**K**) Contour plot of the reconfigurability for the 2D precursor consisting of a semiellipse ribbon and a straight ribbon. (**L**) Optical images and phase diagrams for five representative design points. Scale bars, 2 mm. Photo credit: K.B., Tsinghua University.

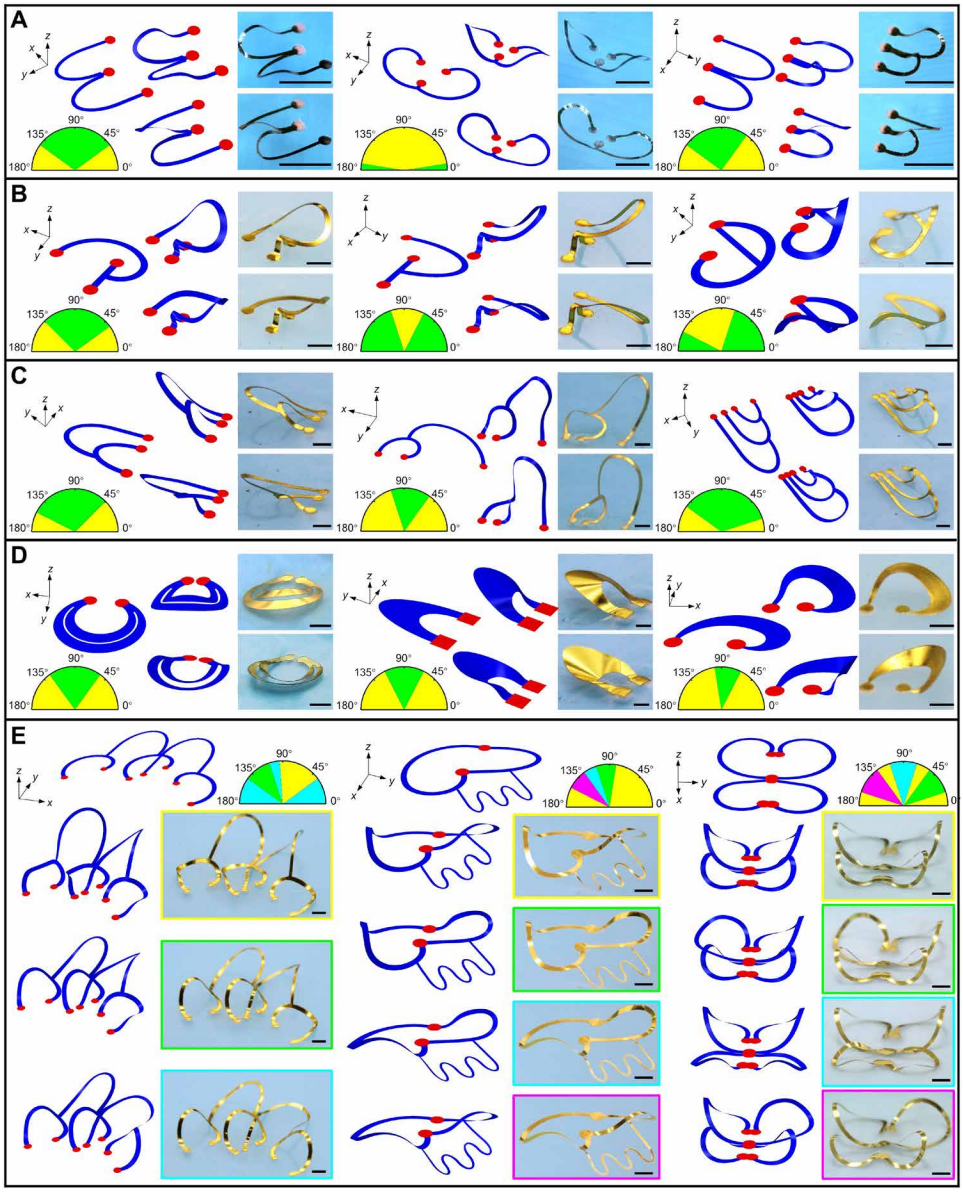

Fig. 3. A variety of 3D reconfigurable mesostructures designed with a bottom-up strategy. (**A** to **C**) 2D precursors, FEA results, optical images, and corresponding phase diagrams of three classes of ribbon-shaped reconfigurable mesostructures. (**D**) Similar results for membrane-shaped reconfigurable mesostructures. (**E**) Similar results for reconfigurable 3D mesostructures with more than two stable configurations. Details about the evolution of deformed configurations during different release processes are in figs. S18 to S21, S25, and S26. In all of the phase diagrams in (A) to (D), the yellow and green regions correspond to the 3D configurations on the top and bottom, respectively. The 3D mesostructures are all made of a bilayer film of Al (1 μm) and PI (25 μm), except for those in (A), which consist of a bilayer of Cu (30 nm) and SU-8 (8 μm). Scale bars, 2 mm. Photo credit: K.B., Tsinghua University.

angle in the range of $36° \leq \varphi \leq 144°$ yields the mode II configuration on the bottom, while the other angles give rise to the mode I configuration on the top, as depicted by the phase diagram. Figure 3B, fig. S20, and movies S2 and S3 provide three examples that introduce straight intersecting ribbons into the elementary ribbon precursors to enhance the reconfigurability and distinction of the two stable configurations. In particular, the reconfigurabilities (K) of the three designs in Fig. 3B are increased to 0.99, 0.75, and 0.99 (from left to right), in comparison to 0.70, 0.64, and 0.84, in the case without the straight intersecting ribbons. Connecting an elementary ribbon to the middle of another ribbon precursor represents another type of bottom-up design strategy, with three typical examples shown in Fig. 3C and fig. S21. Here, the longer curvy ribbon, due to the lower stiffness, mainly follows the spatial bending/twisting deformations of the shorter ribbon at the connection region. The resulting phase diagram is very close to that of the single shorter ribbon (e.g., the semiellipse ribbon in the first design) in the precursor. Membrane-shaped reconfigurable 3D mesostructures can be realized by widening the elementary ribbon precursors. Figure 3D and fig. S22 provide three examples, extended from the ribbon geometries of an arc, a

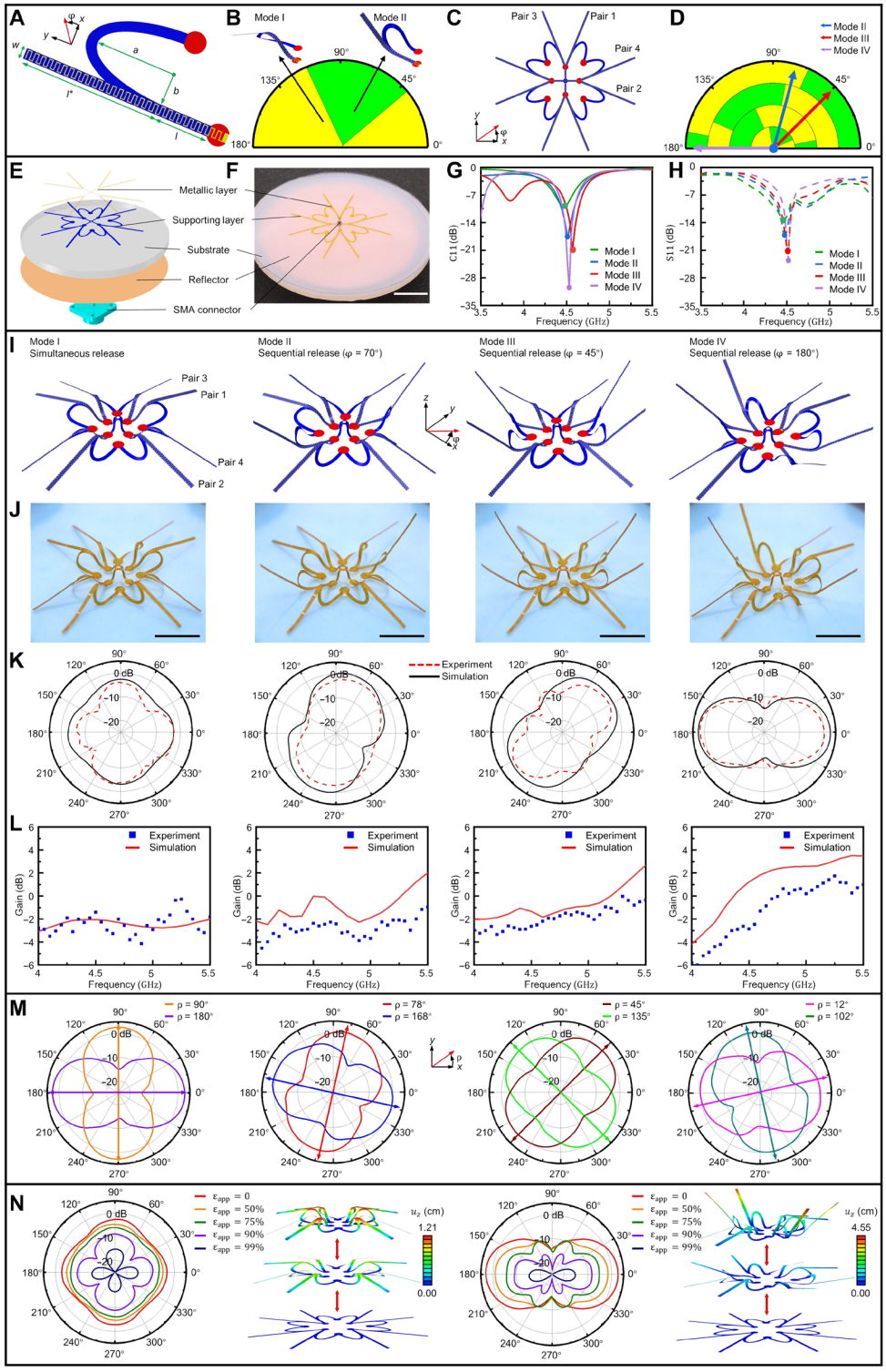

Fig. 4. A multimodal antenna with reconfigurable radiation pattern. (**A** and **B**) 2D precursor and phase diagram of a ribbon-shaped reconfigurable antenna. (**C** and **D**) 2D precursor and phase diagram of a multimodal antenna consisting of four pairs of reconfigurable components in (A). (**E** and **F**) Exploded view illustration and optical images of the antenna. (**G** and **H**) Results of electromagnetic simulations (G) and experimental measurements (H) for the return loss (S11) of the antenna at different operation modes. (**I** and **J**) FEA results and optical images of the antenna at different operation modes. (**K**) H-plane radiation patterns of the antenna at different operation modes. (**L**) Results of electromagnetic simulations and experimental measurements for the gain of the antenna. (**M**) Beam scanning of the antenna enabled by the distinct stable configurations with rotational symmetry and/or mirror symmetry. The corresponding release paths are (90°; 180°), (70°; 160°), (45°; 135°), and (20°; 110°), respectively. (**N**) Tunable H-plane radiation patterns of the antenna at modes I and IV by applying different levels of biaxial stretching to the substrate. The evolving 3D configurations with the biaxial stretching are also included. Scale bars, 2 cm. Photo credit: K.B., Tsinghua University.

semiellipse, and two arcs of different angles/radii, respectively. Additional examples of reconfigurable 3D mesostructures appear in figs. S23 and S24. It is noteworthy that the formation of two distinct 3D configurations in these designs (Fig. 3, A to D) all follows the aforementioned physical mechanism of symmetry break induced by the supporting substrate, with results of three typical examples provided in fig. S25.

The above bottom-up strategy enables a rational design of reconfigurable 3D mesostructures with multiple (≥3) stable configurations. Connecting multiple elementary ribbons with curvy components provides a simple route, but the resulting mesostructures could involve many ribbon segments, as shown in the left panel of Fig. 3E and figs. S26 and S27. In comparison, the combination of two elementary ribbons with properly optimized phase diagrams allows access to substantially simplified, multimodal mesostructures. Figure 3E (middle and right panels) and fig. S28 provide two examples, which consist of only three or four ribbon components, but offer four distinct 3D configurations. Movie S4 illustrates the dynamic process of reconfiguration for the last design in Fig. 3E. An additional example appears in fig. S29, illustrating the strategy to build multimodal reconfigurable mesostructure by patterning elementary ribbon components in a circular array. In all of these examples in Fig. 3, the various stable 3D configurations predicted by FEA always agree well with the experimental results. The phase diagrams provided along with all of those designs serve as a guideline of the 3D reconfiguration through the sequential loading scheme.

Reconfigurable 3D antennas capable of offering distinct radiation patterns

The bottom-up design strategy introduced above allows access to functionally reconfigurable electromagnetic devices through the sequential loading scheme. Figure 4 illustrates a reconfigurable antenna whose radiation pattern can be switched reversibly among many different operation modes. Figure 4A shows the 2D precursor of a bistable whip antenna that consists of a PI supporting layer (thickness t_{PI} = 25 μm) and a metallic layer (thickness t_{Cu} = 6 μm). The key geometrical parameters include the semimajor axis a = 10 mm, semiminor axis b = 4 mm, l = 6 mm, l^* = 25 mm, and width w = 1.2 mm. The phase diagram of this reconfigurable whip antenna is provided in Fig. 4B, where the modes I and II are referred to as the "lay" mode and rise mode, respectively. A distinction of the radiation pattern can be observed between the two operation modes (fig. S30), which can be attributed to the huge difference of the antenna's effective length perpendicular to the substrate surface. Figure 4 (C and D) shows the 2D precursor and phase diagram of a reconfigurable antenna that integrates four pairs of whip antenna components in Fig. 4A to offer multiple operation modes. Figure 4 (E and F) provides an exploded view and an optical image of the antenna, which includes the 2D precursor, the silicone substrate, the metallic reflector, and the subminiature version A (SMA) connector. The S11 parameter curves in Fig. 4F (simulation by commercial software ANSYS HFSS) and Fig. 4G (measurement by network analyzer) illustrate that this antenna has a stable resonant frequency in ~4.5 GHz for different modes. The bandwidth is around 0.3 GHz and shows slight levels of variations during the reconfiguration among different modes. By releasing the prestrained elastomer simultaneously or sequentially along different directions, four typical operation modes can be achieved (Fig. 4, I and J), according to the phase diagram in Fig. 4D. In particular, the simultaneous release leads to the "lay" mode in all of the antenna components, thereby offering an almost homogeneous radiation effect at the H plane. The main direction of the antenna could be adjusted to ρ = 78°, 45°, and 180° through sequential release along φ = 70°, 45°, and 180°, respectively (Fig. 4K). Taking into account the rotational symmetry, the antenna could be adjusted to nine distinct modes in total. For example, the sequential releases with φ = 110°, 160°, and 20° yield the similar radiation patterns like mode II (second panel in Fig. 4K), and the use of φ = 135° also gives a similar radiation pattern like mode III (third panel in Fig. 4K). In all of those operation modes, the antenna provides excellent radiation performances in a broad range of frequency (Fig. 4L). Collectively, the results in Fig. 4M suggest the capability to achieve the beam scanning in discrete mode using a single antenna. Compared with the existing approaches (*56*–*59*), the strategy reported in the current work is unique from the perspective of adjusting the 3D geometry of radiating elements by a mechanically guided reconfiguration process. The resulting beam-scanning antennas that reside on a flexible elastomer substrate can be deformed easily to adapt to complex curvilinear surfaces and/or time-varying surfaces, which are challenging to achieve using the existing approaches. This design concept can be further extended to enable a more densely distributed beam scanning, covering 20 different directions, with a scanning step size of 5° (fig. S31). Stretching the elastomer simultaneously could realize another type of continuous control of radiation pattern (Fig. 4N). The current distributions on the surface of the antenna are shown in fig. S32.

DISCUSSION

In summary, this work introduces a sequential loading scheme and rational bottom-up design strategy to build geometrically reconfigurable mesostructures that can be reshaped among two or multiple stable configurations. Fundamental studies of the physical mechanism of geometric reconfiguration and the phase diagram of sequential loading scheme enable the findings of elementary reconfigurable ribbon precursors that serve as a basis of the bottom-up design strategy. Demonstrations of ~30 diverse examples of reconfigurable 3D mesostructures, including those that consist of very simple ribbon geometries but offer more than three distinct stable configurations, illustrate the powerful capability of the proposed rational design strategy. Functionally reconfigurable 3D antennas with around 10 operation modes suggest opportunities in the development of unusual electromagnetic microdevices. Demonstrated capabilities to achieve reconfigurable radiation patterns and discrete beam scanning using a single antenna suggest the potential to replace the array antenna to realize miniaturized and smart wireless front-end, which could be useful in the scenario of limited design space and deformable carrier.

MATERIALS AND METHODS

Mechanics simulations

FEA using the commercial software Abaqus allowed prediction of the mechanical deformations associated with the 3D reconfiguration. We adopted four-node 2D shell elements (S4R) with bilayer laminates (Cu/PI, Cu/SU-8, and Al/PI) to model the 2D precursors and eight-node 3D solid elements (C3D8R) to model the silicone substrate. Refined meshes ensured the computational accuracy. Results of the linear buckling simulations determined the initial imperfections of postbuckling analyses. We used a hard frictionless contact

model to simulate the mechanical interaction between 2D precursors and the substrate. The elastic modulus (E) and Poisson's ratio (ν) are E_{Cu} = 119 GPa and ν_{Cu} = 0.34 for copper (Cu); E_{PI} = 2.5 GPa and ν_{PI} = 0.34 for PI; $E_{SU\text{-}8}$ = 4.02 GPa and $\nu_{SU\text{-}8}$ = 0.22 for SU-8; E_{Al} = 70 GPa and ν_{Al} = 0.42 for aluminum (Al); and $E_{substrate}$ = 166 kPa and $\nu_{substrate}$ = 0.49 for substrate (Dragon Skin, Smooth-On).

Electromagnetic simulations

FEA using the commercial software HFSS allowed the electromagnetic simulations to calculate the coefficient (S11), impedance (Z11), and radiation pattern of electronic devices. Convergence of mesh sizes was tested to ensure computational accuracy. The model of electromagnetic simulations imported the 3D configurations obtained from the mechanics simulations, and all the metal conducting layers and polymeric supporting layers used layer impedance boundary with prescribed thicknesses. The relative permittivity (ε_r), relative permeability (μ_r), and conductivity (σ) are ε_{r_Cu} = 1, μ_{r_Cu} = 0.999991, and $\sigma_{Cu} = 5.8 \times 10^7$ S/m; ε_{r_PI} = 3.5, μ_{r_PI} = 1, and σ_{PI} = 0 S/m; and $\varepsilon_{r\_Substrate}$ = 2.55, $\mu_{r\_Substrate}$ = 1, and $\sigma_{Substrate} = 2.5 \times 10^{-14}$ S/m.

Fabrication of 3D mesostructures in photodefinable epoxy

Preparation of 3D mesostructures in photodefinable epoxy (SU-8) began with spin coating an ultrathin layer of an adhesion promoter Omnicoat (~17-nm thickness; MicroChem) on a silicon wafer, followed by a layer of SU-8 (~8-μm thickness; MicroChem). Photopatterning the SU-8 defined the geometries of the 2D precursors. Deposition of a layer of Cu (~30-nm thickness) by electron-beam evaporation followed by lithography and wet etching defined the Cu pattern. Immersion in *N*-methyl pyrrolidone (NMP) removed the Omnicoat and released the 2D precursors from the silicon wafer, which were then retrieved by a water-soluble tape [polyvinyl alcohol (PVA); Aquasol Co.], and aligned with a separately prepared polyethylene terephthalate (PET) film of shadow mask (~50 μm) that only exposed the bonding sites. Layers of SiO_2 (100-nm thickness) deposited by electron-beam evaporation through the shadow mask defined the bonding sites, followed by removal of the PET mask. Exposing the prestrained silicone elastomer substrate (Dragon Skin, Smooth-On) and the 2D precursors (on the PVA tap) to ultraviolet (UV)–induced ozone yielded hydroxyl termination on their exposed surfaces. Laminating the tape onto the prestrained silicone elastomer substrate with the exposed SU-8 side down, followed by baking in an oven at 80°C for 10 min, yielded strong chemical covalent bonds between the silicone elastomer substrate and the exposed regions of 2D precursors. After dissolving and washing the PVA tape by hot water, slowly releasing the prestrain in the elastomer along the designed release paths completes the assembly of the 3D mesostructures. Stretching the substrate to initial states again and choosing another strategic release path for the assembly induced the stabilization of a distinct 3D configuration.

Fabrication of 3D mesostructures with submillimeter-scale features

Automated laser cutting (Universal VLS2.30) patterned the 2D precursors [bilayers of aluminum (1 μm)/PI (25 μm)] with desired shapes. A customized four-axis stretcher applied the prestretch to the silicone substrate (1-mm thickness; Dragon Skin, Smooth-On). Pasting commercial adhesive (Super Glue, Gorilla Glue Company) at predefined bonding sites of the prestrained silicone substrate followed by laminating the 2D precursors (with adhesive side down) onto the surface of substrate and curing for ~10 min at room temperature resulted in strong adhesion at the bonding sites. The process of 3D assembly and reconfiguration then followed the same procedures for the SU-8 samples as described above.

Fabrication of 3D reconfigurable antennas

Preparation of 2D precursors began with a commercial flexible printed circuit board (FPCB) [a bilayer of PI (25 μm) and copper (6 μm)], laminated on a water soluble tape (WST) with PI facing the WST. A programmable laser cutting machine (Universal VLS2.30) carved the FPCB into the desired pattern. Photolithographic wet etching patterned the copper layer into designed geometries. Immersing composite in water dissolved WST and separated the 2D precursors. For the reconfigurable energy-harvesting coil antennas, chip LEDs (Red, 0402, APOBICO) and chip capacitors (430PF/50 V, 0402, APOBICO) were then welded with the predesigned electrode of copper layer. Transferring the 2D precursors onto the surface of prestrained silicone substrate, pasting predefined bonding sites by commercial adhesive (Super Glue, Gorilla Glue Company), and curing for ~10 min at room temperature resulted in strong adhesion at the bonding sites. For the reconfigurable communication antennas, a slideable connector and an SMA adapter whose connecting surface stayed at the bottom surface of the substrate were then welded with the predesigned electrode of copper layer. The process of 3D assembly and reconfiguration then followed the same procedures for the SU-8 samples as described above.

Measurement of 3D reconfigurable energy-harvesting antennas

Adhering primary copper coils (LY2026-8, WANLONGJINGYI) on the back of a substrate, and connecting coils with arbitrary function generator (Tektronix AFG2021, 0 to 20 MHz) and wide band amplifier (ATA-122D, 0 to 70 Vpp) served to provide the energy input of coil antennas. The experiment used 3.5 V and 13.56 MHz as the amplitude and frequency of output signal for the arbitrary function generator, and 20 dB for the wide band amplifier. The lightness of LEDs illustrated the distinct operation modes of coil antennas.

Measurement of 3D reconfigurable communication antennas

Connecting the SMA adapter of antenna with a network analyzer (E5071B, Agilent) by a coaxial cable allowed the extraction of the reflection coefficient (S11) and resonant frequency. Next, the SMA adapter of antenna was connected with the signal emission port of a microwave anechoic chamber [working frequency from 800 MHz to 18 GHz; size = 8 m by 4 m by 4 m; homogeneity properties = ±1 dB (axial direction), ±0.5 dB (horizontal direction); shielding properties ≥100 dB (800 MHz to 6 GHz) and ≥90 dB (6 GHz to 18 GHz); AMS8500] (see fig. S33 for details). The radiation pattern was then determined through a measurement in the microwave anechoic chamber using a network analyzer (E5071C, Agilent).

SUPPLEMENTARY MATERIALS

Supplementary material for this article is available at http://advances.sciencemag.org/cgi/content/full/6/30/eabb7417/DC1

REFERENCES AND NOTES

1. C. G. Christodoulou, Y. Tawk, S. A. Lane, S. R. Erwin, Reconfigurable antennas for wireless and space applications. *Proc. IEEE* **100**, 2250–2261 (2012).

2. A. Khidre, K.-F. Lee, F. Yang, A. Z. Elsherbeni, Circular polarization reconfigurable wideband E-shaped patch antenna for wireless applications. *IEEE Trans. Antennas Propag.* **61**, 960–964 (2012).
3. L. Song, A. C. Myers, J. J. Adams, Y. Zhu, Stretchable and reversibly deformable radio frequency antennas based on silver nanowires. *ACS Appl. Mater. Interfaces* **6**, 4248–4253 (2014).
4. W. Lin, H. Wong, Polarization reconfigurable wheel-shaped antenna with conical-beam radiation pattern. *IEEE Trans. Antennas Propag.* **63**, 491–499 (2015).
5. G.-T. Hwang, J. Yang, S. H. Yang, H.-Y. Lee, M. Lee, D. Y. Park, J. H. Han, S. J. Lee, C. K. Jeong, J. Kim, K.-I. Park, K. J. Lee, A reconfigurable rectified flexible energy harvester via solid-state single crystal grown PMN–PZT. *Adv. Energy Mater.* **5**, 1500051 (2015).
6. H. Xu, C. Yu, S. Wang, V. Malyarchuk, T. Xie, J. A. Rogers, Deformable, programmable, and shape-memorizing micro-optics. *Adv. Funct. Mater.* **23**, 3299–3306 (2013).
7. F. López Jiménez, S. Kumar, P. M. Reis, Soft color composites with tunable optical transmittance. *Adv. Opt. Mater.* **4**, 620–626 (2016).
8. F. Zhou, Z. Zhou, J. Chen, T. H. Choy, J. Wang, N. Zhang, Z. Lin, S. Yu, J. Kang, H.-S. P. Wong, Y. Chai, Optoelectronic resistive random access memory for neuromorphic vision sensors. *Nat. Nanotechnol.* **14**, 776–782 (2019).
9. B. Zhu, H. Wang, Y. Liu, D. Qi, Z. Liu, H. Wang, J. Yu, M. Sherburne, Z. Wang, X. Chen, Skin-inspired haptic memory arrays with an electrically reconfigurable architecture. *Adv. Mater.* **28**, 1559–1566 (2016).
10. S. Miao, N. Castro, M. Nowicki, L. Xia, H. Cui, X. Zhou, W. Zhu, S.-j. Lee, K. Sarkar, G. Vozzi, Y. Tabata, J. Fisher, L. G. Zhang, 4D printing of polymeric materials for tissue and organ regeneration. *Mater. Today* **20**, 577–591 (2017).
11. D. Qiao, R. Molfino, S. M. Lardizabal, B. Pillans, P. M. Asbeck, G. Jerinic, An intelligently controlled RF power amplifier with a reconfigurable MEMS-varactor tuner. *IEEE Trans. Microw. Theory Tech.* **53**, 1089–1095 (2005).
12. F. Meng, Y.-M. Hervault, Q. Shao, B. Hu, L. Norel, S. Rigaut, X. Chen, Orthogonally modulated molecular transport junctions for resettable electronic logic gates. *Nat. Commun.* **5**, 3023 (2014).
13. W. Huang, J. Zhou, P. J. Froeter, K. Walsh, S. Liu, M. D. Kraman, M. Li, J. A. Michaels, D. J. Sievers, S. Gong, X. Li, Three-dimensional radio-frequency transformers based on a self-rolled-up membrane platform. *Nat. Electron.* **1**, 305–313 (2018).
14. Z. Tian, B. Xu, B. Hsu, L. Stan, Z. Yang, Y. F. Mei, Reconfigurable vanadium dioxide nanomembranes and microtubes with controllable phase transition temperatures. *Nano Lett.* **18**, 3017–3023 (2018).
15. S. Miyashita, S. Guitron, S. Li, D. Rus, Robotic metamorphosis by origami exoskeletons. *Sci. Robot.* **2**, eaao4369 (2017).
16. C. Wang, K. Sim, J. Chen, H. Kim, Z. Rao, Y. Li, W. Chen, J. Song, R. Verduzco, C. Yu, Soft ultrathin electronics innervated adaptive fully soft robots. *Adv. Mater.* **30**, e1706695 (2018).
17. J. Min, Y. Yang, Z. Wu, W. Gao, Robotics in the Gut. *Adv. Therap.* **3**, 1900125 (2019).
18. V. Magdanz, G. Stoychev, L. Ionov, S. Sanchez, O. G. Schmidt, Stimuli-responsive microjets with reconfigurable shape. *Angew. Chem. Int. Ed.* **53**, 2673–2677 (2014).
19. G. M. Rebeiz, *RF MEMS: Theory, Design, and Technology* (John Wiley & Sons, 2004).
20. T. Yokota, S. Nakano, T. Sekitani, T. Someya, Plastic complementary microelectromechanical switches. *Appl. Phys. Lett.* **93**, 023305 (2008).
21. G. M. Rebeiz, C. D. Patel, S. K. Han, C.-H. Ko, K. M. J. Ho, The search for a reliable MEMS switch. *IEEE Microw. Mag.* **14**, 57–67 (2013).
22. L. Pelliccia, F. Cacciamani, P. Farinelli, R. Sorrentino, High-$\mathcal{Q}$ tunable waveguide filters using ohmic RF MEMS switches. *IEEE Trans. Microw. Theory Tech.* **63**, 3381–3390 (2015).
23. S. Nikolaou, R. Bairavasubramanian, C. Lugo, I. Carrasquillo, D. C. Thompson, G. E. Ponchak, J. Papapolymerou, M. M. Tentzeris, Pattern and frequency reconfigurable annular slot antenna using PIN diodes. *IEEE Trans. Antennas Propag* **54**, 439–448 (2006).
24. J. Perruisseau-Carrier, P. Pardo-Carrera, P. Miskovsky, Modeling, design and characterization of a very wideband slot antenna with reconfigurable band rejection. *IEEE Trans. Antennas Propag.* **58**, 2218–2226 (2010).
25. L. Hinsz, B. D. Braaten, A frequency reconfigurable transmitter antenna with autonomous switching capabilities. *IEEE Trans. Antennas Propag.* **62**, 3809–3813 (2014).
26. A. R. Brown, G. M. Rebeiz, A varactor-tuned RF filter. *IEEE Trans. Microw. Theory Tech.* **48**, 1157–1160 (2000).
27. J. Nath, D. Ghosh, J.-P. Maria, A. I. Kingon, W. Fathelbab, P. D. Franzon, M. B. Steer, An electronically tunable microstrip bandpass filter using thin-film Barium-Strontium-Titanate (BST) varactors. *IEEE Trans. Microw. Theory Tech.* **53**, 2707–2712 (2005).
28. Y.-Y. Bai, S. Xiao, C. Liu, X. Shuai, B.-Z. Wang, Design of pattern reconfigurable antennas based on a two—Element dipole array model. *IEEE Trans. Antennas Propag.* **61**, 4867–4871 (2013).
29. Q. Ge, C. K. Dunn, H. J. Qi, M. L. Dunn, Active origami by 4D printing. *Smart Mater. Struct.* **23**, 094007 (2014).
30. H. Wang, Y. Wang, B. C.-K. Tee, K. Kim, J. Lopez, W. Cai, Z. Bao, Shape-controlled, self-wrapped carbon nanotube 3D electronics. *Adv. Sci.* **2**, 1500103 (2015).
31. Z. Ding, C. Yuan, X. Peng, T. Wang, H. J. Qi, M. L. Dunn, Direct 4D printing via active composite materials. *Sci. Adv.* **3**, e1602890 (2017).
32. K. Liu, J. Wu, G. H. Paulino, H. J. Qi, Programmable deployment of tensegrity structures by stimulus-responsive polymers. *Sci. Rep.* **7**, 3511 (2017).
33. S. J. Mazlouman, A. Mahanfar, C. Menon, R. G. Vaughan, Reconfigurable axial-mode helix antennas using shape memory alloys. *IEEE Trans. Antennas Propag.* **59**, 1070–1077 (2011).
34. S.-H. Byun, J. Y. Sim, Z. Zhou, J. Lee, R. Qazi, M. C. Walicki, K. E. Parker, M. P. Haney, S. H. Choi, A. Shon, G. B. Gereau, J. Bilbily, S. Li, Y. Liu, W.-H. Yeo, J. G. McCall, J. Xiao, J.-W. Jeong, Mechanically transformative electronics, sensors, and implantable devices. *Sci. Adv.* **5**, eaay0418 (2019).
35. X. Zhang, Z. Yu, C. Wang, D. Zarrouk, J.-W. T. Seo, J. C. Cheng, A. D. Buchan, K. Takei, Y. Zhao, J. W. Ager, J. Zhang, M. Hettick, M. C. Hersam, A. P. Pisano, R. S. Fearing, A. Javey, Photoactuators and motors based on carbon nanotubes with selective chirality distributions. *Nat. Commun.* **5**, 2983 (2014).
36. Y. Fang, Y. Jiang, H. A. Ledesma, J. Yi, X. Gao, D. E. Weiss, F. Shi, B. Tian, Texturing silicon nanowires for highly localized optical modulation of cellular dynamics. *Nano Lett.* **18**, 4487–4492 (2018).
37. W. Xu, T. Li, Z. Qin, Q. Huang, H. Gao, K. Kang, J. Park, M. J. Buehler, J. B. Khurgin, D. H. Gracias, Reversible MoS_2 origami with spatially resolved and reconfigurable photosensitivity. *Nano Lett.* **19**, 7941–7949 (2019).
38. H. Irschik, A review on static and dynamic shape control of structures by piezoelectric actuation. *Eng. Struct.* **24**, 5–11 (2002).
39. B. Watson, J. Friend, L. Yeo, Piezoelectric ultrasonic micro/milli-scale actuators. *Sens. Actuators A Phys.* **152**, 219–233 (2009).
40. A.-G. Olabi, A. Grunwald, Design and application of magnetostrictive materials. *Mater. Design* **29**, 469–483 (2008).
41. Y. Kim, H. Yuk, R. Zhao, S. A. Chester, X. Zhao, Printing ferromagnetic domains for untethered fast-transforming soft materials. *Nature* **558**, 274–279 (2018).
42. R. Pelrine, R. Kornbluh, G. Kofod, High-strain actuator materials based on dielectric elastomers. *Adv. Mater.* **12**, 1223–1225 (2000).
43. S. J. Mazlouman, M. Soleimani, A. Mahanfar, C. Menon, R. G. Vaughan, Pattern reconfigurable square ring patch antenna actuated by hemispherical dielectric elastomer. *Electron. Lett.* **47**, 164–165 (2011).
44. X. Zhang, C. L. Pint, M. H. Lee, B. E. Schubert, A. Jamshidi, K. Takei, H. Ko, A. Gillies, R. Bardhan, J. J. Urban, M. Wu, R. Fearing, A. Javey, Optically-and thermally-responsive programmable materials based on carbon nanotube-hydrogel polymer composites. *Nano Lett.* **11**, 3239–3244 (2011).
45. C. Yu, Z. Duan, P. Yuan, Y. Li, Y. Su, X. Zhang, Y. Pan, L. L. Dai, R. G. Nuzzo, Y. Huang, H. Jiang, J. A. Rogers, Electronically programmable, reversible shape change in two-and three-dimensional hydrogel structures. *Adv. Mater.* **25**, 1541–1546 (2013).
46. J. C. Breger, C. Yoon, R. Xiao, H. R. Kwag, M. O. Wang, J. P. Fisher, T. D. Nguyen, D. H. Gracias, Self-folding thermo-magnetically responsive soft microgrippers. *ACS Appl. Mater. Interfaces* **7**, 3398–3405 (2015).
47. E. C. Davidson, A. Kotikian, S. Li, J. Aizenberg, J. A. Lewis, 3D printable and reconfigurable liquid crystal elastomers with light-induced shape memory via dynamic bond exchange. *Adv. Mater.* **32**, 1905682 (2019).
48. A. Kotikian, C. M. Mahan, E. C. Davidson, J. M. Muhammad, R. D. Weeks, C. Daraio, J. A. Lewis, Untethered soft robotic matter with passive control of shape morphing and propulsion. *Sci. Robot.* **4**, eaax7044 (2019).
49. M. D. Dickey, Stretchable and soft electronics using liquid metals. *Adv. Mater.* **29**, 1606425 (2017).
50. B. L. Cumby, G. J. Hayes, M. D. Dickey, R. S. Justice, C. E. Tabor, J. C. Heikenfeld, Reconfigurable liquid metal circuits by Laplace pressure shaping. *Appl. Phys. Lett.* **101**, 174102 (2012).
51. S. Xu, Z. Yan, K.-I. Jang, W. Huang, H. Fu, J. Kim, Z. Wei, M. Flavin, J. M. Cracken, R. Wang, A. Badea, Y. Liu, D. Xiao, G. Zhou, J. Lee, H. U. Chung, H. Cheng, W. Ren, A. Banks, X. Li, U. Paik, R. G. Nuzzo, Y. Huang, Y. Zhang, J. A. Rogers, Assembly of micro/nanomaterials into complex, three-dimensional architectures by compressive buckling. *Science* **347**, 154–159 (2015).
52. Y. Zhang, Z. Yan, K. Nan, D. Xiao, Y. Liu, H. Luan, H. Fu, X. Wang, Q. Yang, J. Wang, W. Ren, H. Si, F. Liu, L. Yang, H. Li, J. Wang, X. Guo, H. Luo, L. Wang, Y. Huang, J. A. Rogers, A mechanically driven form of Kirigami as a route to 3D mesostructures in micro/nanomembranes. *Proc. Natl. Acad. Sci. U.S.A.* **112**, 11757–11764 (2015).
53. Y. Zhang, F. Zhang, Z. Yan, Q. Ma, X. Li, Y. Huang, J. A. Rogers, Printing, folding and assembly methods for forming 3D mesostructures in advanced materials. *Nat. Rev. Mater.* **2**, 17019 (2017).
54. W. Pang, X. Cheng, H. Zhao, X. Guo, Z. Ji, G. Li, Y. Liang, Z. Xue, H. Song, F. Zhang, Z. Xu, L. Sang, W. Huang, T. Li, Y. Zhang, Electro-mechanically controlled assembly of reconfigurable 3D mesostructures and electronic devices based on dielectric elastomer platforms. *Natl. Sci. Rev.* **7**, 342–354 (2020).
55. H. Fu, K. Nan, W. Bai, W. Huang, K. Bai, L. Lu, C. Zhou, Y. Liu, F. Liu, J. Wang, M. Han, Z. Yan, H. Luan, Y. Zhang, Y. Zhang, J. Zhao, X. Cheng, M. Li, J. W. Lee, Y. Liu, D. Fang, X. Li,

Y. Huang, Y. Zhang, J. A. Rogers, Morphable 3D mesostructures and microelectronic devices by multistable buckling mechanics. *Nat. Mater.* **17**, 268–276 (2018).
56. M. Euler, V. F. Fusco, Frequency selective surface using nested split ring slot elements as a lens with mechanically reconfigurable beam steering capability. *IEEE Trans. Antennas Propag.* **58**, 3417–3421 (2010).
57. S. G. Hay, S. L. Smith, G. P. Timms, J. W. Archer, Three-shaped-reflector beam-scanning pillbox antenna suitable for mm wavelengths. *IEEE Trans. Antennas Propag.* **59**, 2495–2501 (2011).
58. V. Pacheco-Peña, V. Torres, B. Orazbayev, M. Beruete, M. Navarro-Cía, M. Sorolla, N. Engheta, Mechanical 144 GHz beam steering with all-metallic epsilon-near-zero lens antenna. *Appl. Phys. Lett.* **105**, 243503 (2014).
59. D. K. Karmokar, K. P. Esselle, S. G. Hay, Fixed-frequency beam steering of microstrip leaky-wave antennas using binary switches. *IEEE Trans. Antennas Propag.* **64**, 2146–2154 (2016).

Acknowledgments
Funding: Y.Z. acknowledges support from the National Natural Science Foundation of China (# 11722217), the Tsinghua University Initiative Scientific Research Program (# 2019Z08QCX10), and the Henry Fok Education Foundation and the Tsinghua National Laboratory for Information Science and Technology. **Author contributions:** Y.Z. designed and supervised the research; Y.Z. and K.B. led the structural designs, mechanics modeling, and FEA predictions of reconfigurable mesostructures with assistance from F.Z. and Y.H.; K.B. led the microfabrication work of mesostructures, with assistance from X.C., Z.X, and F.Z.; Y.Z. and K.B. led the device designs, electromagnetic modeling, and analyses of reconfigurable antennas, with assistance from W.H., L.S., F.L., and X.L.; K.B. led the fabrication and experimental characterization of reconfigurable antennas, with the assistance from X.C. and H.S.; Y.Z. and K.B. wrote the text and designed the figures. All authors commented on the paper. **Competing interests:** The authors declare that they have no competing interests. **Data and materials availability:** All data needed to evaluate the conclusions in the paper are present in the paper and/or the Supplementary Materials. Any additional datasets, analysis details, and material recipes may be requested from the authors. Correspondence and requests for materials should be addressed to Y.Z.

Submitted 15 March 2020
Accepted 5 June 2020
Published 22 July 2020
10.1126/sciadv.abb7417

Citation: K. Bai, X. Cheng, Z. Xue, H. Song, L. Sang, F. Zhang, F. Liu, X. Luo, W. Huang, Y. Huang, Y. Zhang, Geometrically reconfigurable 3D mesostructures and electromagnetic devices through a rational bottom-up design strategy. *Sci. Adv.* **6**, eabb7417 (2020).